Supplemental Information

Photothermal Conversion of Gold Nanoparticles for Fast and Uniform Laser Warming of Vitrified Biomaterials

Yilin Liu[a], Joseph Kangas[a], Yiru Wang[a], Kanav Khosla[a], Jacqueline Pasek-Allen[a], Aaron Saunders[b], Steven Oldenburg[b], John Bischof[*,a,c,d]

[a]Department of Mechanical Engineering, University of Minnesota, Minneapolis, MN 55455, USA.
[b]NanoComposix, 4878 Ronson Court Suite K, San Diego, CA 92111, USA.
[c]Department of Biomedical Engineering, University of Minnesota, Minneapolis, MN 55455, USA.
[d]Director, Institute of Engineering in Medicine, University of Minnesota, Minneapolis, MN 55455, USA.
E-mail: Bischof@umn.edu

Table of Contents

Figure S9. The status of laser warmed droplets changes according to the different input laser energy

S1. UV-vis-NIR extinction spectra and TEM of GNPs

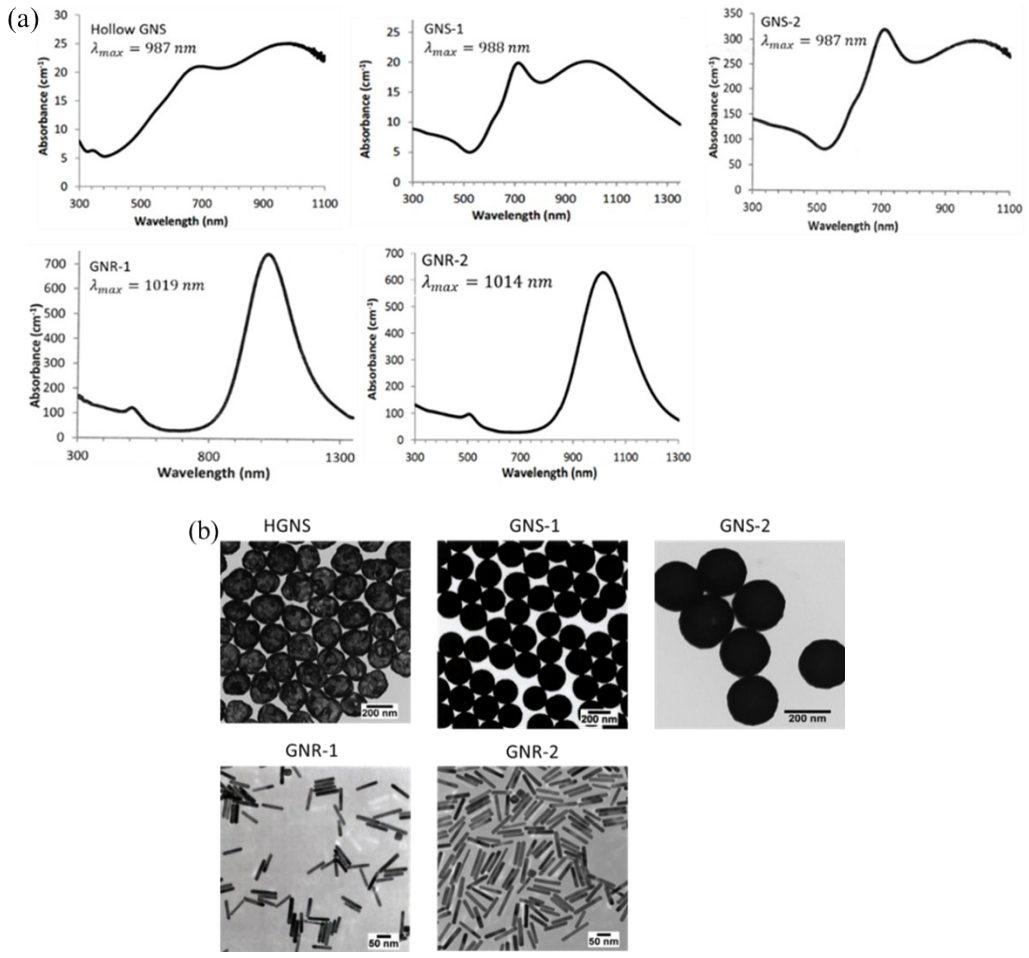

Figure S1. The (a) absorption spectra and (b) TEM images of the GNSs and GNRs (provided by nanoComposix). The absorbance in (a) refers to the extinction normalized by pathlength of light.

S2. Experimental and modeling methods

S2.1 Experimental photothermal conversion efficiencies of GNPs and solutions

The experimental photothermal conversion efficiencies of GNPs ($\eta_{exp,GNP}$) and their solutions ($\eta_{exp,tot}$) are characterized by the cuvette heating system. This system was calibrated to obtain the correlation between heat generation rate due to laser irradiation in the bulk solution (Q_{tot}) and the maximum temperature difference (ΔT_{max}) between the solution and the environment. The black ink[2, 3] and ultra-pure water[4] can be both approximated as pure absorbers of light (i.e. with negligible scattering) and were used for calibrating the cuvette system. The laser beam's power

loss (P_{loss}) through the aqueous black ink solution was then assumed to equal the heat generation in the solution due to light absorption (Q_{tot}). The example of temperature recording in calibration experiments is shown in Figure S2(a) and the fitting curve of the correlation is provided in Figure S2(b). When the system reaches a thermal steady state (e.g. plateaued temperature curve in Figure S2(a)), the heat dissipation rate is equal to the heat generation in the cuvette system by both laser heating and stir bar's work. There is a linear relationship between the heat dissipation rate and the temperature difference between the solution and environment[5]. By reducing the stir bar's effect as shown in Figure S2(b), the heat generation rate of the GNP solutions by laser heating (Q_{tot}) in this steady state thus can be fit as

$$Q_{tot} = P_{loss} = 14.302\ [mW\ K^{-1}] * (\Delta T_{max} - \Delta T_0)\ \ [mW] \qquad (S1)$$

where ΔT_{max} and ΔT_0 are the steady-state (maximum) temperature difference between the liquid and environment with and without laser irradiation, respectively. The fitting curve in Figure S2(b) does not pass the origin because there was still an appreciable steady-state temperature increase (ΔT_0) due to the stir bar's work even without laser heating. It is noted that tuning up the stirring speed causes an increase in ΔT_0.

However, when characterizing the GNP solution, the Q_{tot} incorporates both water and GNPs' absorption of direct irradiation and reabsorption of the scattered light. This can cause the overestimation of the photothermal conversion efficiency of GNPs. To address this, the effect of water's absorption of 1064 nm laser energy was accounted for as noted below. This is necessary because water has greater absorption at 1064 nm light than at 532 nm which was used in our previous study[6]. Additionally, the reabsorption of scattering was decoupled from direct absorption by Monte Carlo modeling as detailed in Methods.

During the laser heating measurement, the steady-state radiative transfer equation can be written as[4]

$$(dI_\lambda)_{net} = (dI_\lambda)_{abs} + (dI_\lambda)_{out-sca} + (dI_\lambda)_{em} + (dI_\lambda)_{in-sca} \qquad (S2)$$

where the left term is the net radiative intensity (I) change at 1064 nm wavelength within a finite light path length (ds), while the terms on the right side (in sequence) are specific radiative intensity change terms due to absorption, out-scattering, emission, and in-scattering radiation, respectively. The emission and in-scattering of GNPs can be ignored when compared with much larger absorption and out-scattering[7]. Thus, the radiative transfer equation can be reduced and calculated as:

$$(dI_\lambda)_{net} = (dI_\lambda)_{abs} + (dI_\lambda)_{out-sca} = I(s)\ *\ \mu_{t,tot}\, ds \qquad (S3)$$

where $\mu_{t,tot}$ is the total extinction coefficient of the GNP solution. For the diluted system, the $\mu_{t,tot}$ can be calculated as

$$\mu_{t,tot} = \mu_{t,water} + \mu_{t,GNP} \qquad (S4)$$

Therefore, the power loss of the laser beam (i.e. integrating laser intensity over its beam area) caused by GNPs and water is proportionally allocated by the ratio of $\mu_{t,water}$:$\mu_{t,GNP}$. The portions of the laser's power loss by water ($P_{loss,water}$) and GNPs ($P_{loss,GNP}$) can thus be calculated as

$$P_{loss,water} = P_{loss,tot} * \frac{\mu_{t,water}}{\mu_{t,tot}} \quad (S5)$$

and

$$P_{loss,GNP} = P_{loss,tot} * \frac{\mu_{t,GNP}}{\mu_{t,tot}} \quad (S6)$$

where $P_{loss} = P_{in} - P_{out}$ is the laser beam's total power loss through the solution in the cuvette. The P_{in} and P_{out} are the power of the laser going into and out of the solution between the cuvette walls (Figure 2(a)). They were calculated from the measured laser power in front of ($P_{in}^{'}$) and out of ($P_{out}^{'}$) the cuvette (Figure 2(a)) in the laser path. Note that the calculated total transmittance through the single cuvette wall from the air to the waterside by Fresnel's law is 95.38%, which was validated by experimental measurement allowing us to write:

$$P_{in} = P_{in}^{'} * 95.38\% \quad (S7)$$

and

$$P_{out} = \frac{P_{out}^{'}}{95.38\%} \quad (S8)$$

By integrating Equation (S3) over the light path length and beam area, the $\mu_{t,tot}$ is related to the laser beam's power (P) by

$$\mu_{t,tot} = \frac{1}{L} \ln\left(\frac{P_{out}}{P_{in}}\right) \quad (S9)$$

where L is the path length (1 cm) of the laser beam through the solution. If the solution is pure water without GNPs, we can measure the ultra-pure water's extinction coefficient, $\mu_{t,water} = 0.147388\ cm^{-1}$.

The heat generation by water's absorption of laser energy (Q_{water}), including both absorption and reabsorption of scattering, is equal to the laser beam's power loss by water's portion ($P_{loss,water}$) because the pure liquid is a non-scattering absorber[4]. Thus, the heat generation by water can be calculated as

$$Q_{water} = P_{loss,water} = (P_{in} - P_{out}) * \frac{\mu_{t,water}}{\mu_{t,tot}} \quad (S10)$$

Therefore, the heat generation caused only by GNPs can be calculated as

$$Q_{GNP} = Q_{tot} - Q_{water} \quad (S11)$$

The Q_{GNP} still includes the heat generation due to GNPs' reabsorption of scattered light.

The estimated photothermal conversion efficiencies of the GNP and the whole solution from the measurement were

$$\eta_{exp,GNP} = \frac{Q_{GNP}}{P_{loss,\ GNP}} \quad (S12)$$

and

$$\eta_{exp,tot} = \frac{Q_{tot}}{P_{loss,tot}} \qquad (S13)$$

both of which were overestimated to a certain extent because the measured heat generation incorporated the re-absorption of the scattered light in the bulk solution.

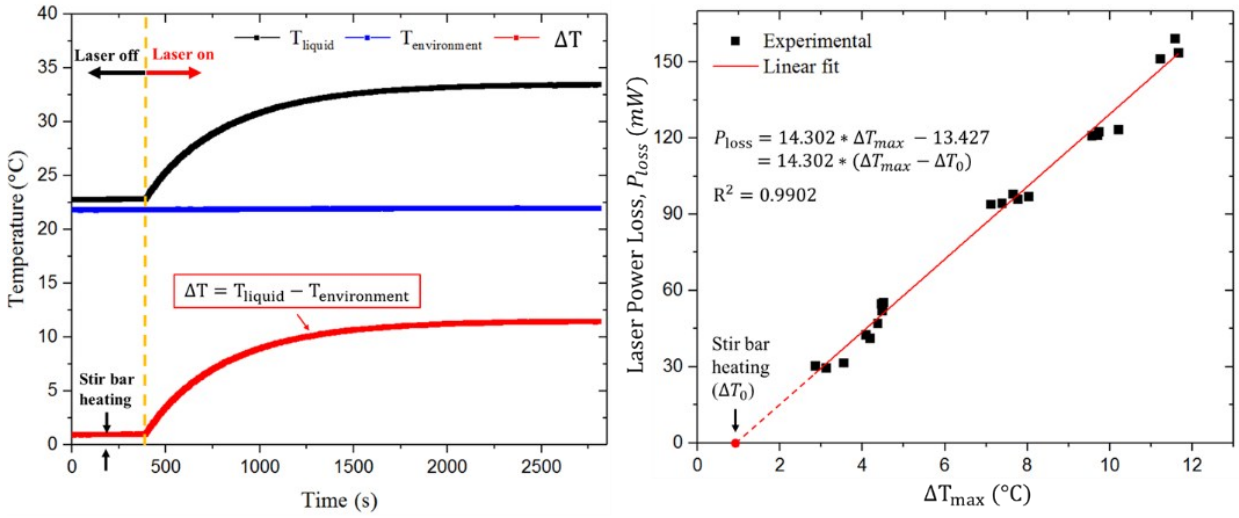

Figure S2. Calibration of the heat generation rate by laser heating of black-ink aqueous solution (approximated as a pure absorber). (a) Example of recording temperature of environment ($T_{environment}$) and the solution in the cuvette (T_{liquid}) and their difference (ΔT) during the cuvette heating experiments. (b) Fitting of the heat generation rate in the GNP solution due to laser irradiation as a function of maximum temperature difference before (ΔT_0) and during (ΔT_{max}) laser heating. The stirring speed was kept constant for all the calibration experiments at 150 rpm.

S2.2 Modeling and validation

(1) Anisotropy factor for Monte Carlo modeling

The scattering anisotropy factor of the GNRs was assumed to be 0.25, which was obtained by fitting the experimental angular scattering data in the reference work[8] with the Henyey-Greenstein phase function for GNRs with sizes close to those used in this study. The GNSs are strongly scattering, especially when the size is > 200 nm[9]. In that report[9], the anisotropy factor for the silica-cored GNS was almost 0 near its resonance wavelength (~1145 nm). It is, therefore, reasonable to assume the anisotropy factor of the GNSs used in this study to be 0 at 1064 nm, which is also near their resonance wavelengths in the NIR (~987nm in Figure S1(a)).

The scattering of the medium was also considered when modeling GNR-2s in the egg white medium. As reported in the literature[10], the scattering by egg white is mainly caused by clusters of proteins, which produced Rayleigh scattering as long as no severe denaturation had occurred. The experimental temperature in this study was kept less than 37 $^{\circ}C$ to avoid protein denaturation. Thus, the anisotropy factor of the egg white medium was assumed to be 0. The anisotropy factor of the

GNP-loaded egg white medium is averaged proportionally by the scattering coefficient from egg white and GNPs.

(2) Modeling the rewarming of droplet

In COMSOL simulation, the thermal properties of 2M (20.15 wt%) PG solution are summarized in Table S1 and justified below. The thermal conductivity, specific heat, and density of the liquid CPA solutions were calculated by the weighted average. As for the vitreous status, the thermal conductivity and density were assumed as constant from room temperature to the vitreous status. This assumption is based on the reported findings that the thermal conductivity of vitreous glycerol[11] and the density of other vitreous CPA solutions[12] keep almost constant during vitrification. For specific heat, however, there can be a ~ 56% jump during the vitrification transition[12, 13]. The transition temperature of the 2M PG was assumed to be -105 °C[14].

Table S1. Thermal properties of the droplet used in the COMSOL modeling.

Thermal conductivity ($W \cdot m^{-1} \cdot K^{-1}$)	Specific heat capacitance ($J \cdot kg^{-1} \cdot K^{-1}$)	Density ($kg \cdot m^3$)
0.5159	4019 ($T > -105\ °C$); 1768.5 ($T < -105\ °C$)	1008

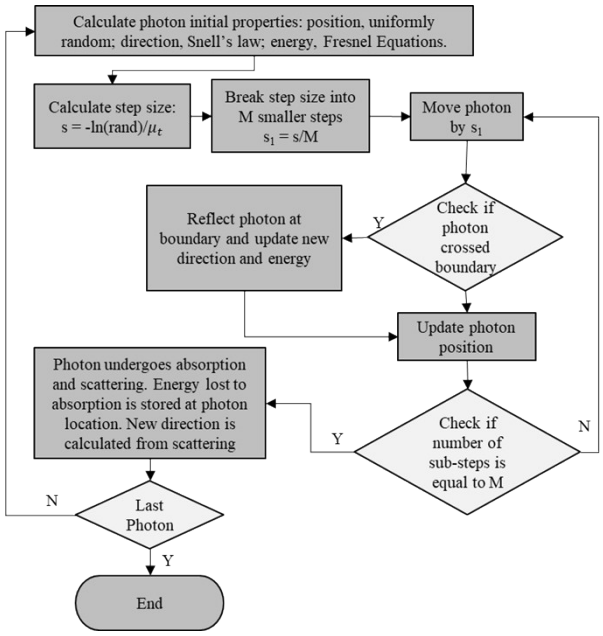

Figure S3. Accounting for the singularity of the photon step in the bottom edge of the hemispherical droplet in Monte Carlo modeling during the laser warming.

(3) Optimizing the optical properties for droplet rewarming by Monte Carlo modeling

When changing the optical properties of the droplets to achieve optimal uniformity in laser heating, different values of γ_{tot} and the non-dimensional $\mu_{a,tot} * R$ were assumed and input into the Monte Carlo model to compute the SAR distribution in the droplet. The parameters for the photons and boundary conditions remained the same as those for GNR-2 and GNS cases (shown in Table 3).

Here the use of non-dimensional γ_{tot} and $\mu_{a,tot} * R$ can be justified by simultaneously normalizing the droplet size and the photon step ($-\frac{\ln(RND)}{\mu_{t,tot}}$, RND: random number between 0 and 1)[1] by the droplet's radius, thus getting the unit droplet with radius at 1 (dimensionless) and the photon step as dimensionless $-\frac{\ln(RND)}{\mu_{t,tot} * R}$. Thus, the computed SAR for the unit droplet is related to $\mu_{t,tot} * R$ and the overall photothermal efficiency, $\eta_{tot} = \frac{\mu_{a,tot}}{\mu_{t,tot}}$, both of which are dimensionless. By multiplying those two variables and applying $\eta_{tot} = \frac{1}{1+\gamma_{tot}}$, it is reasonable to use the γ_{tot} and $\mu_{a,tot} * R$ as dimensionless variables to characterize the optical properties of the unit droplet.

(4) Validation of the Monte Carlo modeling

To validate the effectiveness of the Monte Carlo modeling, we used Monte Carlo codes to model the two extreme cases, no scattering and high scattering, and compared the predicted SAR with the analytical solutions from the well-established reference by AJ Welch et al[1]. It was assumed that a semi-infinite turbid slab was irradiated by a collimated laser with a matched refractive index at boundaries.

For the no scattering case which assumed that $\mu_{a,tot} = 15\ cm^{-1}\ and\ \mu_{s,tot} = 0$, the distribution of the laser fluence rate follows Beer-Lambert law and normalized by the maximum inlet rate as[1]:

$$\phi_t(z) = \exp\left(-\mu_{t,tot} * z\right) \tag{S14}$$

where z is the distance to the slab's irradiated surface along the collimated light transport direction.

For another high scattering case, it was assumed that $\mu_{a,tot} = 1\ cm^{-1}$, $\mu_{s,tot} = 100\ cm^{-1}$, g=0.1. The diffusion theory[1] can apply since its mean free path of light (i.e. $\frac{1}{\mu_{t,tot}} \cong 0.0099\ cm$) is much smaller than the slab's width (assumed semi-infinite). In this high-scattering limit case where $\mu_{a,tot} \ll \mu_{s,tot}(1-g)$, the distribution of the laser energy fluence rate is[1]

$$\phi_t(z) = \frac{5}{1+\frac{2*\mu_{a,tot}}{\mu_{eff}}} \exp\left(-\mu_{eff} * z\right) - 2 * \exp\left(-\mu_{t,tot} * z\right) \tag{S15}$$

where the effective extinction coefficient is $\mu_{eff} = \sqrt{3\mu_{a,tot} * (\mu_{a,tot} + (1-g) * \mu_{s,tot})}$ and the irradiation energy is set as 1. For both cases, the fluence rate of the absorbed laser energy (i.e. SAR) is

$$SAR = \phi_{abs}(z) = \mu_{a,tot} * \phi_t(z) \tag{S16}$$

Figure S4 shows that in both cases, the SARs normalized by their maximum as predicted by Monte Carlo codes are comparable to those solutions from the AJ Welch et al.[1] thereby validating our codes.

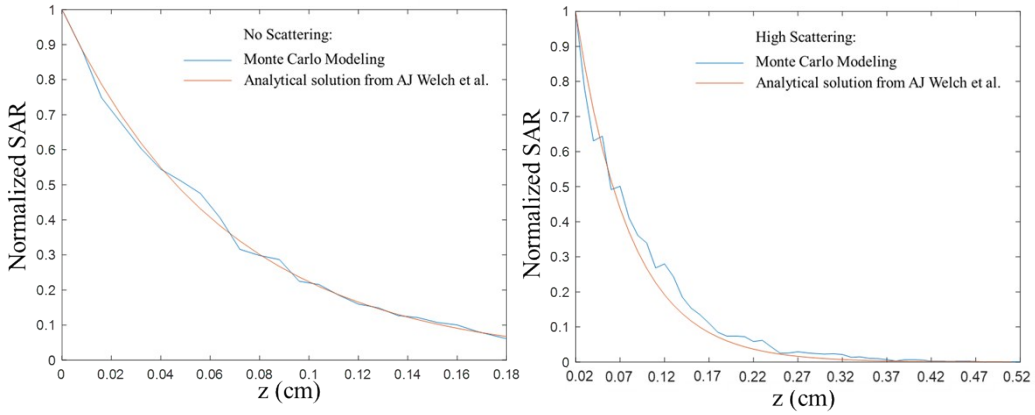

Figure S4. Validation of the Monte Carlo model by comparing with solutions from AJ Welch et al.[1]

S2.3 Comparing data analysis methods for characterizing GNPs in the bulk solution

There are multiple methods for characterizing the photothermal conversion efficiencies. The methods proposed by H. Richardson et al.[15], D. Roper et al.[5] and Z. Qin et al.[6] all used heat transfer analysis in laser-gold solution heating experiments to obtain the optical properties of the single GNP. However, details in their data analysis varied, as discussed below.

(1) The heat transfer equation changes in different systems

To calculate the steady-state heat generation rate of the GNP solutions during laser heating, Richardson et al.[15] and D. Roper et al.[5] fit the cooling curves of the solution to obtain the heat dissipation rate from the system to the environment, while Z. Qin et al.[6] used the equivalent electrical heating to calibrate the solution's heat generation rate as a function of temperature increment from laser-off to laser-on steady states. The nanoparticle suspension systems reported by H. Richardson et al.[15](droplet) and D. Roper et al.[5] (sample in the cell) are smaller in scale (~1 mm) than that described by Z. Qin et al.[6] (cuvette system similar to ours, 1 cm). As will be discussed below, the heat transfer equations are different in the different systems (i.e. droplet, cell container, cuvette with stir bar). Therefore, the cooling curve fitting method in Richardson et al.[15](droplet) and D. Roper et al.[5] cannot be directly applied to the cuvette heating experiments without modification.

To achieve uniform heating in the cuvette, the stir bar should be working during heating and cooling. The energy input by the stir bar into the suspensions is an additional heat source in the heat equation. Thus, the equations for the photothermal efficiency in nanofluid droplets [15] and cell[5] systems cannot be directly applied to the cuvette system with a stirring bar. In the cuvette system, the heat transfer equation can be defined as

$$\sum_i m_i C_{p,i} \frac{dT}{dt} = Q_{GNP} + Q_{medium} + Q_{stir} - Q_{ext} \qquad (S17)$$

where m_i, $C_{p,i}$, and T are the mass, heat capacity and temperature the system, respectively; Q_{NPs}, Q_{medium} are heat generation terms due to laser energy absorption by GNPs and liquid medium,

respectively; Q_{stir} is the heat generation due to work done by the stirring bar, which is constant for a constant stirring speed; Q_{ext} is the heat dissipation to the environment and can be approximated as $Q_{ext} = hA(T - T_{environment})$. Here, the Q_{stir} is the extra term which does not exist in the heat transfer equations in H. Richardson et al.[15] and D. Roper et al.[5].

Assuming that $\theta^* = \frac{T - T_{environment}}{T_{ss} - T_{environment}}$ and $\tau_s \equiv \frac{\sum_i m_i C_{p,i}}{hA}$, where T_{ss} is the steady-state temperature of the liquid during laser heating, the equation (S17) becomes

$$\frac{d\theta^*}{dt} = \frac{1}{\tau_s}\left[\frac{Q_{GNP} + Q_{medium} + Q_{stir}}{hA(T_{ss} - T_{environment})} - \theta^*\right] \quad (S18)$$

During the cooling period after blocking the laser, the equation (S17) becomes

$$\frac{d\theta^*}{dt} = \frac{1}{\tau_s}\left[\frac{Q_{stir}}{hA(T_{ss} - T_{environment})} - \theta^*\right] \quad (S19)$$

The initial condition is $\theta^* = 1$ at the beginning of cooling. Letting $c_0 = \frac{Q_{stir}}{hA(T - T_{environment})}$ as constant, the solution to equation (S19) will be

$$\theta^* = c_0 + (1 - c_0)\exp\left(-\frac{t}{\tau_s}\right) \quad (S20)$$

The constant c_0 can be calculated by equilibrating the system at the temperature of T_0 after turning on the stir bar but without laser heating. At steady state, the heat generation by the only heat source of stirring will be balanced by heat loss to the environment. Thus,

$$c_0 = \frac{Q_{stir}}{hA(T - T_{environment})} = \frac{hA(T_0 - T_{environment})}{hA(T - T_{environment})} = \frac{T_0 - T_{environment}}{T - T_{environment}} \quad (S21)$$

Therefore, when fitting the cooling data from the cuvette experiment to get τ_s, the expression for the y-axis should be $ln(\theta^* - c_0)$ instead of $\ln \theta^*$ used in the two former reports[5, 15].

To address the above problem, the cuvette heating system was calibrated either by equivalent electrical heating in our previous report[6] or by laser heating of the blank ink aqueous solution in this study. So the heat dissipation rate from the cuvette to the environment was directly acquired as a function of temperature difference (ΔT) for the heat transfer analysis.

Additionally, the energy balance of the two calibration methods was compared by laser heating pure water in the cuvette system, and was calculated as $\frac{heat\ generation}{laser\ beam's\ power\ loss} \times 100\%$. The calibration method in this study has a better energy balance (108.48%±7.78%) than that in the previous study[6] (128.07% ±9.19%). It may be because there could be more measurement error introduced by the additional instruments (e.g. electrical current and voltage measurement) in the equivalent electrical heating method[6].

(2) Background heat generation by medium's absorption of laser energy

The background heat generation due to the medium's (e.g. water) absorption of the laser energy can cause the overestimation of the photothermal conversion efficiency of GNPs. This effect was considered in D. Roper et al.[5] while being ignored by the other two reports[6, 15]. This study also considered the heat generation due to laser absorption by the medium when measuring the GNPs' photothermal conversion efficiency. However, there is still a difference in extracting the medium's absorption of laser energy. The following discussion demonstrates that the analysis method used in this study is more accurate than that in the previous report[5] and has fewer constraints.

D. Roper et al.[5] determined the water's heat generation ($Q_{water}^{'}$) in a GNP solution by independently measuring pure water in the heating setup. So the heat generation of water in the independent measurement was

$$Q_{water}^{'} = P_{loss} = P_0\left(1 - \exp\left(\mu_{t,water} * l\right)\right) \quad (S22)$$

where P_0 is the laser energy reaching the front side of the system.

However, in this study, the water's heat generation in GNP solutions during laser beam excitation is directly deduced from the radiative transfer equation and is calculated in equation (S10) with higher accuracy. It can be further recast as

$$Q_{water} = P_{loss,tot} * \frac{\mu_{t,water}}{\mu_{t,tot}} = P_0\left(1 - \exp\left(\mu_{t,tot} * l\right)\right) * \frac{\mu_{t,water}}{\mu_{t,tot}} \quad (S23)$$

It can be noted that $Q_{water}^{'}$ in equation (S22) can markedly deviate from Q_{water} in equation (S23) unless one of the following restrictions is satisfied: (1) $\frac{\mu_{t,water}}{\mu_{t,tot}}$ of the GNP solution is close to 1, and/or (2) $\mu_{t,water}$ is very small in the system.

(3) Reabsorption of scattered light in the solutions

The reabsorption of scattered light in a GNP solution also tends to cause the overestimation of the photothermal conversion efficiency of the GNPs, depending on the particle type and the dimensional scale of the system (GNP solutions). The overestimation effect will be more apparent in characterizing higher scattering nanoparticles, such as GNSs. In addition, the reabsorption of scattering tends to be more significant in larger-scale systems due to the longer pathlength of the photons when compared with a smaller system. For example, in the cuvette heating experiment (1 cm dimension for 1 mL solution), the GNSs can be overestimated for ~30% in the experimental photothermal conversion efficiency while the GNRs were less impacted. But for smaller droplets (e.g. modeling 2 mm droplets' rewarming), the difference in the total laser energy absorption rate in GNS and GNR case is minimal (56.3% vs. 53.5%), though there is a large difference in temperature distribution. Therefore, when characterizing GNPs in the small systems[5, 15], the effects of reabsorption of scattered light on measuring the total heat generation can be negligible. In contrast, as for the cuvette system (1 cm scale), those effects can be more important when characterizing GNPs' optical properties. Herein, Monte Carlo modeling was performed to trace the photons through the solution and record the reabsorbed scattering energy inside the system. This is detailed in the Methods.

S2.4 Relationship between optical properties measured by UV-vis-NIR spectrometer and cuvette system

Extinction, extinction coefficient and extinction cross section all describe the optical extinction properties of the GNPs or their solutions at a specific wavelength (e.g. 1064 nm). The extinction of GNPs (A_{GNP}) for 1 cm light pathlength, was measured in a UV-vis-NIR spectrophotometer by subtracting the background extinction of pure medium (A_{medium}) from that of the total solution (A_{tot}) as follows

$$A_{GNP} = A_{tot} - A_{medium} \quad (S24)$$

The extinction coefficient, $\mu_{t,tot}$, for the GNP solution was measured in the cuvette system and obtained by Equation (S9). The extinction cross section, C_{ext}, for a single GNP was characterized using the cuvette heating system with Monte Carlo analysis (Method). The relationship between $\mu_{t,tot}$ and C_{ext} is shown in Equation (3) from Table 2. Essentially, both A_{tot} and $\mu_{t,tot}$ can describe the transmissivity of light through the solution in a cuvette with the light's pathlength (L) as 1 cm. Supposing that the inlet light's intensity is I_{in}, the transmitted light's intensity, I_{out}, can be calculated by both A_{tot} and $\mu_{t,tot}$ as

$$I_{out} = I_{in} * 10^{-A_{tot}} = I_{in} * e^{-\mu_{t,tot} * L} \quad (S25)$$

Thus, the relationship between A_{tot} and $\mu_{t,tot}$ is

$$A_{tot} = \mu_{t,tot} * L * \log_{10} e \quad (S26)$$

For pure medium without GNPs, equation (S26) can be written as

$$A_{medium} = \mu_{t,medium} * L * \log_{10} e \quad (S27)$$

By plugging Equations (3), (S26-S27), the Equation (S24) becomes

$$A_{GNP} = (\mu_{t,tot} - \mu_{t,medium}) * L * \log_{10} e = N * C_{ext} * L * \log_{10} e \quad (S28)$$

where N is the number concentration of the GNPs in the solution.

S3. Effects of CPA on the photothermal properties of GNPs

S3.1 Effects of 2M PG on the extinction spectra of GNPs

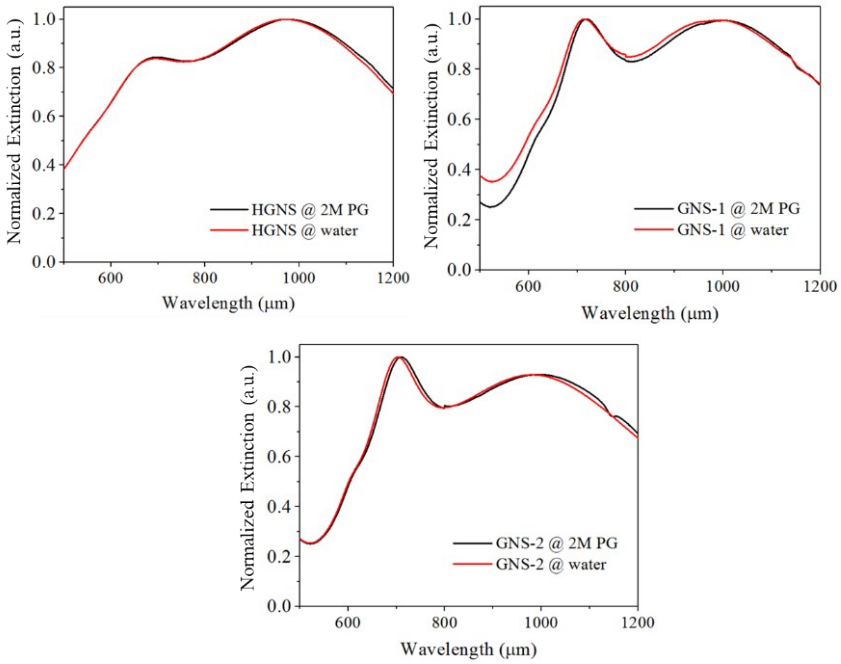

Figure S5. Comparison of the absorption spectra of GNR-2 in water and 2M PG solutions. Test on GNR-1 was conducted due to the lack of enough available samples. The extinction spectra plot was normalized by the peak extinction.

S3.2 Effects of egg white medium on the extinction spectrum of GNR-2

Since the GNRs and GNSs have nearly identical surface coatings and similar resonance peak near 1064 nm, their interactions with the medium are expected to be similar. Especially, the coatings play a major role in their dispersion stability[16, 17], thus affecting those interactions. As a result, further characterization of the optical properties in egg white medium (this section) and stability test in CPAs (section S4) were only conducted on the GNR-2 type, as a model for all GNPs. The experimental trend obtained from GNR-2 is expected to be transferrable to other GNPs.

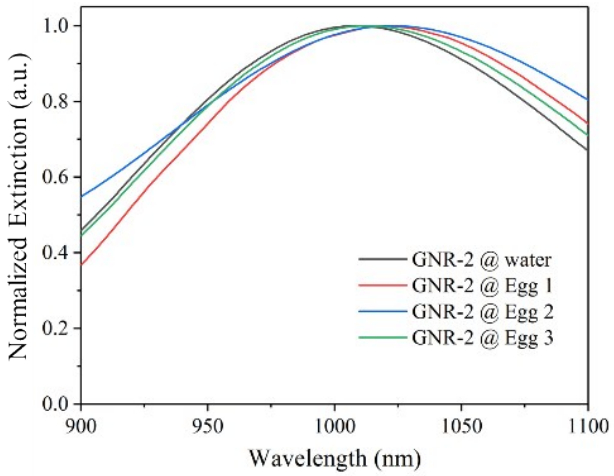

Figure S6. Comparison of the absorption spectra (900 – 1100 nm) of GNR-2 in water and different egg white solutions. The spectra outside of the 900 – 1100 nm had a large variation between different GNP-egg white solutions, which was possibly due to contamination and/or variation of contents between eggs. The extinction spectra plot was normalized by the peak extinction.

S4. Characterizing the dispersion stability against sedimentation of low-concentration (non-interacting) GNR-2s

Besides optical properties, the dispersive stability of the GNR-2 was also tested, which is important to determine their consistent photothermal performance over time. Precipitation of GNR-2 in biological media can adversely impact their photothermal performance due to the non-uniform optical properties of the bulk suspension. Nonstable particles are also vulnerable to aggregation, which can induce shifted and diminished extinction peaks depending on the size and geometry of the aggregation parcels[18].

Ligands on the surface of GNPs are known to increase their dispersion stability in solutions and/or to add functionality. PEG is an excellent example of this as it is both biocompatible and hydrophilic, and such polymers are often used for surface functionalization.[19] Herein, GNRs were coated in PEG with MW 5000 Da. Unfortunately, CPAs are not mimics of aqueous solutions because their large organic, salt, and/or sugar components can change NP dispersion stability significantly[20]. PG is less polar but more viscous than water, and it has different molecular geometry which decreases its affinity for PEG, which in turn may change how PEGylated NPs are stabilized in solution.[21-24] Sugars may also change PEG's affinity for the solution. As there is various literature pointing to PG and sugars changing the stability of NP dispersions, we tested the PEGylated GNR-2s in various CPAs to determine their settling rates.

S4.1 Method of stability test

The stability test against sedimentation was conducted by monitoring the extinction of GNR-2 solutions (A_{tot}) at 1064 nm when the GNRs were dispersed in CPAs. The stock solution of GNR-2, as received, was diluted in each of the different solvents (ultrapure water as control, 2M PG, 6M PG, 13.1M PG, 2M PG + 1M trehalose, and 2M PG + 1M sucrose) to a final concentration of 6.0E9 particles mL^{-1} and vortexed. Each condition was repeated 3 times. 1 mL of each solution

was pipetted into the cuvette (1 cm light path length). The extinction at 1064 nm was measured in the same setup as in Figure 2(a) but without thermocouples and stirring. To avoid remixing by shaking, the GNPs solutions were handled very gently and slowly to measure the extinction in the cuvette setup. In between measurement, the solutions were kept static at room temperature. The extinction was measured every 24 hours over 14 days. Additionally, aggregation during the storage time was tested by measuring their UV−vis−NIR spectra via a Cary 7000 UV−vis−NIR spectrophotometer (Agilent Technologies) before and after the extinction monitoring test. For comparison, the values of extinction were normalized by the one measured on the first day. The over 14 days of testing timescale aims for the future application in the large-scale high-throughput vitrifying and rewarming of biomaterials where GNPs in CPA solutions need to remain shelf-stable.

S4.2 Dispersion stability against sedimentation of the non-interacting GNRs' in CPAs

Figure S7 compares the effect of the CPA components to the GNR-2s' dispersion stability, specifically concentrations (molarity) of PG and sugar additives. To preclude GNR-2 aggregation, the UV-vis-NIR extinction spectrum of the GNR-2s before and after the stability test was compared (Figure S8). The overlapping spectrum curves in Figure S8 demonstrate monodisperse GNR-2s without aggregation in all the studied solutions. As suggested in Figure S7, in the low-concentration GNR-2 solutions (6.0E9 particles mL^{-1}), the GNR-2's sedimentation rate was highest in aqueous solutions, followed by 13.1M PG, 2M and 6M PG, and 2M PG with 1M trehalose or sucrose.

It is important to note that the concentration of the tested GNR-2s was low, 6.0E9 particles mL^{-1}, to minimize the amount of material used and to prevent saturation of the UV-vis-NIR spectra measurement. This concentration effectively prevents particles from interacting over the timescales tested. Otherwise, at higher concentrations, PEG chains may interact and condense together, creating agglomerates. At low concentrations, however, PEG chains can only condense around the particle to which they are attached. Therefore, the settling rate is mainly due to particle affinity with the solvent rather than the competition between aggregation increasing mass and affinity of the solvent to the polymer chain.[25] The addition of 2M or 6M PG lowered the precipitation speed, whose relative decrease in extinction was less than 5% in 14 days when compared with the over 12% drop of extinction in water (control). This is possible because PEG and PG both have polar (ether) and nonpolar (aliphatic chain) areas which may also increase PEG stability in PG solutions. 13.1M PG (i.e. pure PG with a trace amount of water) decreased the stability of the suspension but still had better stability than in pure water. This is possibly due to the higher viscosity of the high-polarity PG as discussed below. It is also noted that adding either sugar (1 M trehalose or 1 M sucrose) into 2M PG can slightly improve the dispersion stability of the GNR-2 regardless of the sugar types, which is discussed further below.

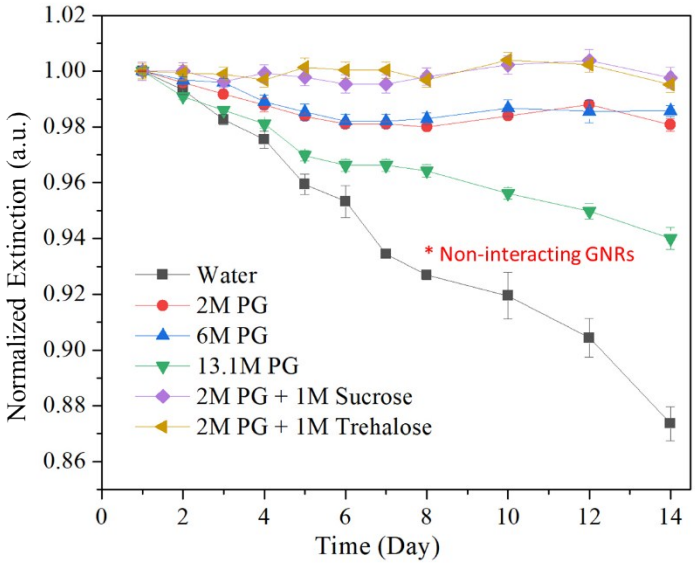

Figure S7. Evolution of the extinction at 1064 nm of the non-interacting GNR-2s suspended in CPAs.

The scale analysis of the precipitation Peclet number (Pe) may also help explain the sedimentation rate of GNR-2 in various solutions. A smaller Peclet number indicates better diffusive movement and thus more uniform suspension. When a Peclet number is large, convective movement dominates and the suspension tends to become stratified. The Stokes velocity can be used to determine the final settling velocity (U_{settle}) of the GNR-2s in Newtonian solvents[26, 27], which is defined as:

$$U_{settle} = \frac{(m_{GNP} - \rho_{solvent} V_{GNP}) g}{f} \qquad (S29)$$

where m_{GNP} and V_{GNP} are the mass and volume of GNR-2; f is friction coefficient; g is the acceleration of gravity, and $\rho_{solvent}$ is the solvent density. The Peclet number can be determined as

$$Pe = \frac{L\, U_{settle}}{D_{diffuse}} = \frac{(m_{GNP} - \rho_{solvent} V_{GNP}) gL}{D_{diffuse} \times f} \qquad (S30)$$

where $D_{diffuse}$ is the diffusion coefficient and L is the characteristic length of the GNR-2 in the solvents.

The densities of PG and water are close (PG: 1.036 g cm^{-3}; water: 1 g m^{-3}) while the viscosity of PG is significantly larger than that of water (PG: 0.042 $Pa \cdot s$; water: 0.00089 $Pa \cdot s$). It is assumed that in different solvents, the change in L of the PEGylated GNR-2 varies negligibly compared to the changes in $D_{diffuse}$ and f. Thus, viscosity and polarity of the solvent may determine the Pe. Adding sugars (trehalose and sucrose) will potentially increase the viscosity while decreasing the polarity of the solvents. In general, the overall f of PEGylated GNR-2s is positively correlated to viscosity, while the $D_{diffuse}$ has a negative relationship with it. As for polarity, water is more polar

than PG molecules, so PEG tends to have stronger hydrodynamic interaction with water-enriched solvents and thus higher diffusion[28]. Also, as discussed in the previous section, a combination of high polar water and less polar PG even better disperses PEG chains, which may increase the diffusion of PEGylated GNR-2 and thus $D_{diffuse}$. Therefore, when looking at equation (S30), there may be an optimal condition that combines highly polar water and highly viscous PG solvents with sugar additives, such as near 2M PG with 1M sugar, so that the GNR-2s' Peclet number is as small as possible and the stability against sedimentation is optimized.

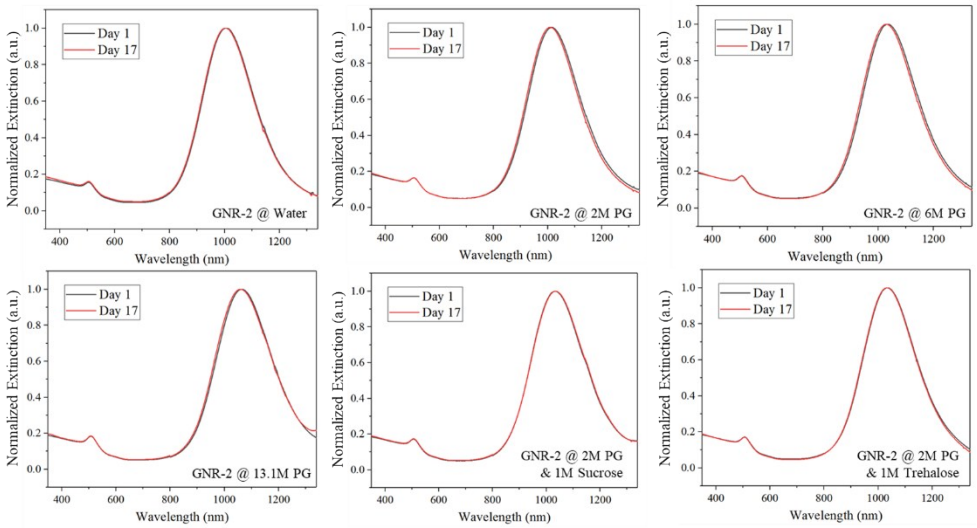

Figure S8. Comparison of the extinction spectrum of the GNR-2 overtime in different solutions.

S5. Experimental fast cooling and laser warming of droplets

S5.1 Experimental method

The fast cooling and laser warming of droplets was conducted as described by our previous study[14, 29] with only a few modifications in parameters. The scheme is illustrated in Figure 1(a). Briefly, a 0.5 μL droplet loaded with 30% (w/w) glycerol, 10% (w/w) trehalose, and diluted GNRs (unknown concentration) was pipetted onto the blade of a modified cryotop. For fast cooling, an automated control system was programmed to enables the cryotop to cool the droplet by immersing and equilibrating it in the liquid nitrogen for about 10s. For rewarming, the control system was also able to automatically raise the droplet, align it at the focus of the 1064 nm Nd:YAG laser (iWeld 980 Series, 120 J, LaserStar Technologies, FL, USA), and trigger the laser with a single pulse. The laser beam radiated from the top of the droplet with a beam size larger than the droplet size. The laser energy was changed by changing the voltage (V) and pulse width (ms). The entire cooling and rewarming process was recorded by a camera while the ms laser warming process was blocked to avoid potential damages to the camera.

S5.2 Discussion on over-warmed, under-warmed, and well-warmed cases

The success of rewarming is determined when the droplets remain clear (without white ice spots) and intact (without boiling or cracking) by looking at their recordings after laser heating. The output status of the rewarmed GNP-loaded droplets changes with the input laser energy as illustrated in Figure S9. There are different types of failed rewarming due to non-uniform heating,

including cracking, boiling, and ice crystallization inside the droplets. However, having the GNP type and concentration, and the laser input match with each other is critical for successful warming. The successfully rewarming case is shown in Figure 1(c) while the over-wared (with boiling) and under-warmed (with significant ice crystallization) cases are shown in Figure 1(b) and (c), respectively.

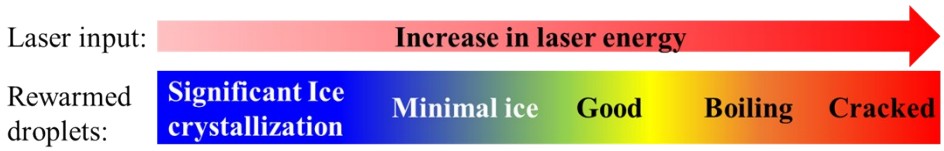

Figure S9. The status of laser warmed droplets changes according to the different input laser energy.

References:

1 A. J. Welch and M. J. Van Gemert, *Optical-thermal response of laser-irradiated tissue*, Springer, 2011.
2 A. Dimofte, J. C. Finlay and T. C. Zhu, *Phys. Med. Biol.*, 2005, **50**, 2291.
3 V. G. Peters, D. Wyman, M. Patterson and G. Frank, *Phys. Med. Biol.*, 1990, **35**, 1317.
4 M. F. Modest, *Radiative heat transfer*, Academic press, 2013.
5 D. K. Roper, W. Ahn and M. Hoepfner, *J. Phys. Chem. C*, 2007, **111**, 3636-3641.
6 Z. Qin, Y. Wang, J. Randrianalisoa, V. Raeesi, W. C. Chan, W. Lipiński and J. C. Bischof, *Sci. Rep.*, 2016, **6**, 29836.
7 P. K. Jain, K. S. Lee, I. H. El-Sayed and M. A. El-Sayed, *J. Phys. Chem. B*, 2006, **110**, 7238-7248.
8 G. S. He, J. Zhu, K. T. Yong, A. Baev, H. Cai, R. Hu, Y. Cui, X. H. Zhang and P. Prasad, *J. Phys. Chem. C*, 2010, **114**, 2853-2860.
9 Y. Hu, R. C. Fleming and R. A. Drezek, *Opt. Express*, 2008, **16**, 19579-19591.
10 J. W. Pickering, *J. Photochem. Photobiol. B: Biol.*, 1992, **16**, 101-111.
11 J. H. Choi and J. C. Bischof, *Int. J. Heat Mass Transfer*, 2008, **51**, 640-649.
12 M. L. Etheridge, Y. Xu, L. Rott, J. Choi, B. Glasmacher and J. C. Bischof, *Technology*, 2014, **2**, 229-242.
13 K. Trachenko and V. Brazhkin, *Phys. Rev. B*, 2011, **83**, 014201.
14 K. Khosla, Y. Wang, M. Hagedorn, Z. Qin and J. Bischof, *ACS nano*, 2017, **11**, 7869-7878.
15 H. H. Richardson, M. T. Carlson, P. J. Tandler, P. Hernandez and A. O. Govorov, *Nano Lett.*, 2009, **9**, 1139-1146.
16 C. Fang, N. Bhattarai, C. Sun and M. Zhang, *Small*, 2009, **5**, 1637-1641.
17 R. Pamies, J. G. H. Cifre, V. F. Espín, M. Collado-González, F. G. D. Baños and J. G. de la Torre, *J. Nanopart. Res.*, 2014, **16**, 2376.
18 M. Loumaigne, C. Midelet, T. Doussineau, P. Dugourd, R. Antoine, M. Stamboul, A. Débarre and M. H. Werts, *Nanoscale*, 2016, **8**, 6555-6570.
19 B. D. Chithrani, A. A. Ghazani and W. C. W. Chan, *Nano Letters*, 2006, **6**, 662-668.
20 L. Amornkitbamrung, J. Kim, Y. Roh, S. H. Chun, J. S. Yuk, S. W. Shin, B.-W. Kim, B.-K. Oh and S. H. Um, *Langmuir*, 2018, **34**, 2774-2783.
21 I. Lázár and H. Szabó, *Gels*, 2018, **4**, 55.
22 I. Palabiyik, Z. Musina, S. Witharana and Y. Ding, *J. Nanopart. Res.*, 2011, **13**, 5049.
23 J. J. Scheepers, E. Muzenda and M. Belaid, *J. Clean Energy Technol.*, 2015, **3**, 282-286.
24 P. L. Gould, M. Goodman and P. A. Hanson, *Int. J. Pharm.*, 1984, **19**, 149-159.

25 L. Wu, J. Zhang and W. Watanabe, *Adv. Drug Del. Rev.*, 2011, **63**, 456-469.
26 P. Cheng and H. Schachman, *Journal of polymer science*, 1955, **16**, 19-30.
27 K. Benes, P. Tong and B. J. Ackerson, *Physical Review E*, 2007, **76**, 056302.
28 K. Shimada, H. Kato, T. Saito, S. Matsuyama and S. Kinugasa, *J. Chem. Phys.*, 2005, **122**, 244914.
29 K. Khosla, L. Zhan, A. Bhati, A. Carley-Clopton, M. Hagedorn and J. Bischof, *Langmuir*, 2018, **35**, 7364-7375.